1.5.5.10 Electronic structures

Introduction

Since the last review [88W1] no further polarised neutron measurements have been published. However, there have been some photoemission and positron investigations of the band structure of $L2_1$ and $C1_b$ compounds.

X_2YZ X = 3d, Y = 3d

X = 1B: Cu
Y = 7A: Mn
Z = 3B: Al

Photoelectron spectroscopy has been undertaken on Cu_2MnAl. However, it must be emphasised that Cu_2MnAl is particularly difficult to prepare in single crystal form.

Table 118. Binding energies *E* in eV. Accuracy ± 0.1 eV. Standard level $Al2_p$ = 75.0 eV. Data was taken for two orientations of Cu_2MnAl [90S4].

	Plane (111)		Plane (100)	
Level	As received	Cleaned	As received	Cleaned
Al2p	75.0	75.0	75.0	75.0
Mn2p	642.5	642.5	642.5	639.8
Cu2p	932.8	932.8	932.7	933.7
O1s	532.3	532.5	532.6	531.1
C1s	285.3	285.2	284.6	284.6

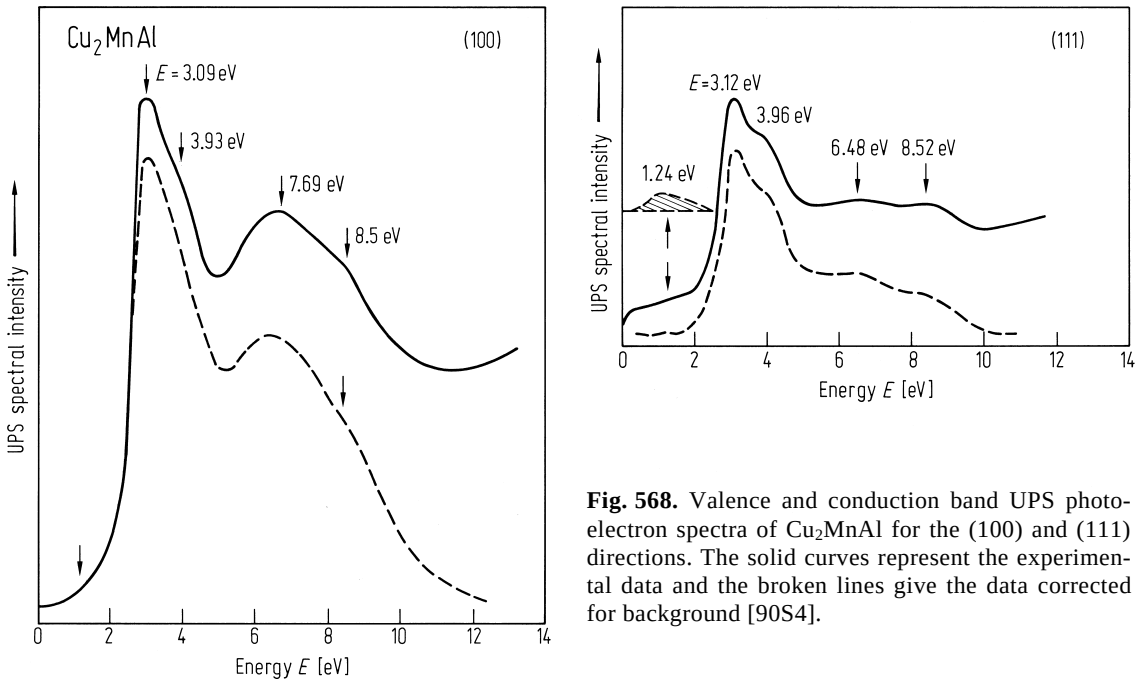

Fig. 568. Valence and conduction band UPS photoelectron spectra of Cu_2MnAl for the (100) and (111) directions. The solid curves represent the experimental data and the broken lines give the data corrected for background [90S4].

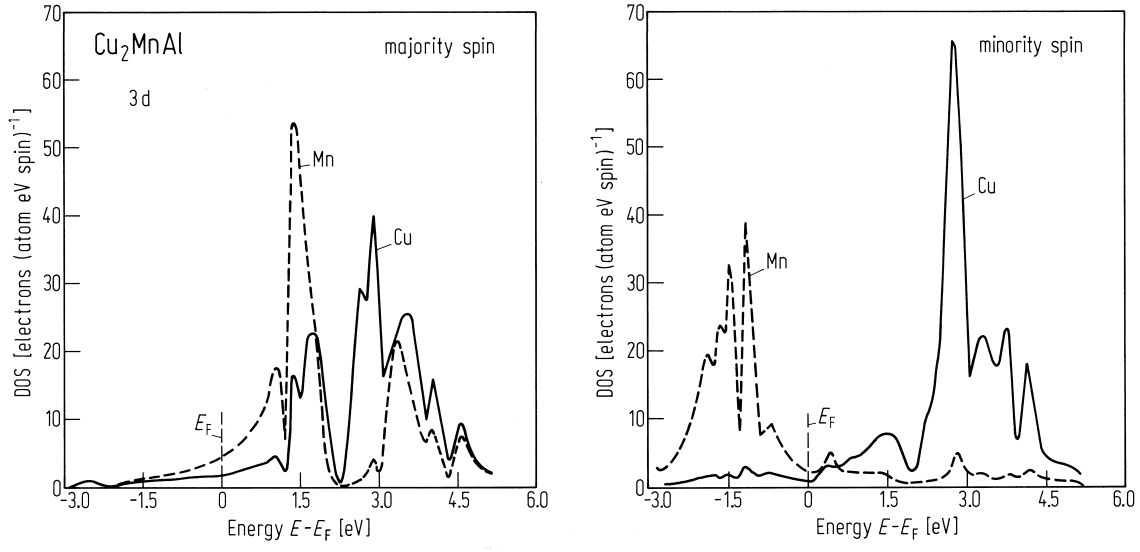

Fig. 569. Contribution of the densities of states of the d components of Cu_2MnAl from the Mn and Cu sites [90S4].

X = 7A: Mn; 8A: Fe, Co
Y = 7A: Mn; 8A: Fe
Z = 3B: Al; 4B: Si

The systematic changes in the band structure upon changing the elements XYZ have been investigated using X-ray spectroscopy. The results have been compared with the prediction of band models. The results indicate that the d-band energies BCD (Fig. 575) which arise from resonant scattering of nearly free Al or Si electrons by 3d states decrease with higher atomic number Fe–Co–Cu. The peaks in the silicon compounds occur at lower energies than in the aluminium compounds. This is expected since Al has lower electro-negativity than Si.

Table 119. A summary of the alloys investigated in Figs. 571 to 574 [83B1].

Structure	A_2	B_2	$D0_3$, $L2_1$		
Formula	T	TAl	X_2YZ	X_2YZ	X_2YZ
Site A, C	T	T	X	p_X	p_Y
B	T	Al	Y	[μ_B]	[μ_B]
D	T	Al	Z		
	V	VAl			
	Cr				
			Mn_2MnSi	0.5	0.8
	Fe	FeAl	Fe_2FeAl	1.6	2.2
			Fe_2FeSi	1.2	2.4
		CoAl	Co_2MnAl	0	?
			Co_2MnSi	0.8	3.6
		NiAl			
			Cu_2MnAl	0	3.5

Table 120. A summary of the X-ray transitions of the elements indicated in Table 119 [83B1]. VB: valence band.

Locus momentum	T-metal	*E* [eV]	Al/Si	*E* [eV]
s, d	VB (3d) → $2p_{3/2}$	600…800	VB (s, d) → 2p	70…120
p			VB (p) → 1s	≈ 1500/1800

Table 121. Distribution probabilities of elements on the lattice sites A, B and C as indicated in Fig. 1.

Alloy	Probability	[84Z1]	[79M1]
Co_2MnSi	$P_{\alpha Si}$	0	
	$P_{\beta Si}$	0.12 ± 0.01 X-ray diffr.	
	$P_{\gamma Si}$	0.91 ± 0.05	
	$P_{\alpha Mn}$	0.19 ± 0.02	
	$P_{\beta Mn}$	0.81 ± 0.08 EXAFS	
	$P_{\gamma Mn}$	0	
$Fe_{2.4}Mn_{0.6}Al$	$P_{\alpha Al}$	0.05 ± 0.01	0.04
	$P_{\beta Al}$	0.25 ± 0.02 X-ray diffr.	0.15 X-ray diffr.
	$P_{\gamma Al}$	0.61 ± 0.03	0.72
	$P_{\alpha Mn}$	0.34 ± 0.04	0.04
	$P_{\beta Mn}$	0.66 ± 0.07 EXAFS	0.39 neutron diffr.
	$P_{\gamma Mn}$	0	0.11

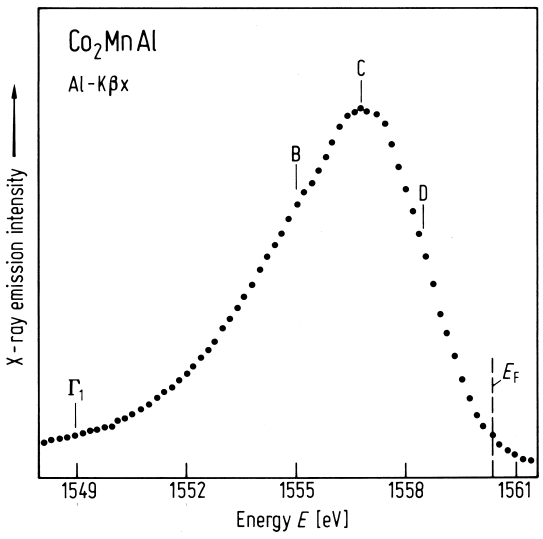

Fig. 570. Observed X-ray emission bands from Al in Co_2MnAl. The bottom of the band is denoted by Γ and the Fermi energy by E_F. The labels B, C and D indicate possible resonant scattering of the nearly free Al electrons by the 3d transition states [83B1].

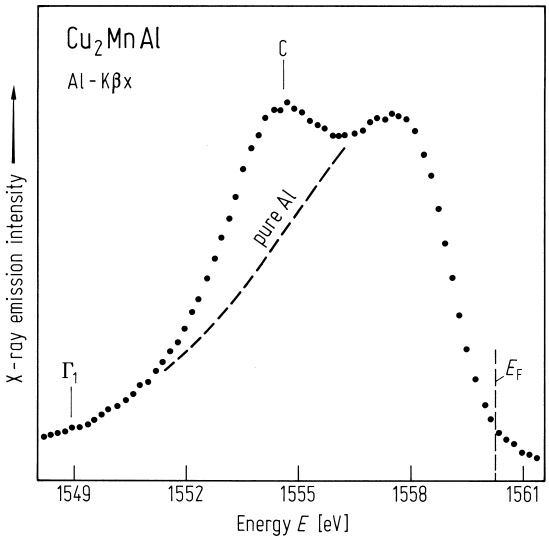

Fig. 571. Observed X-ray emission bands from Al in Cu_2MnAl. The bottom of the band is denoted by Γ and the Fermi energy by E_F. The label C indicates possible resonant scattering of the nearly free Al electrons by the 3d transition states [83B1].

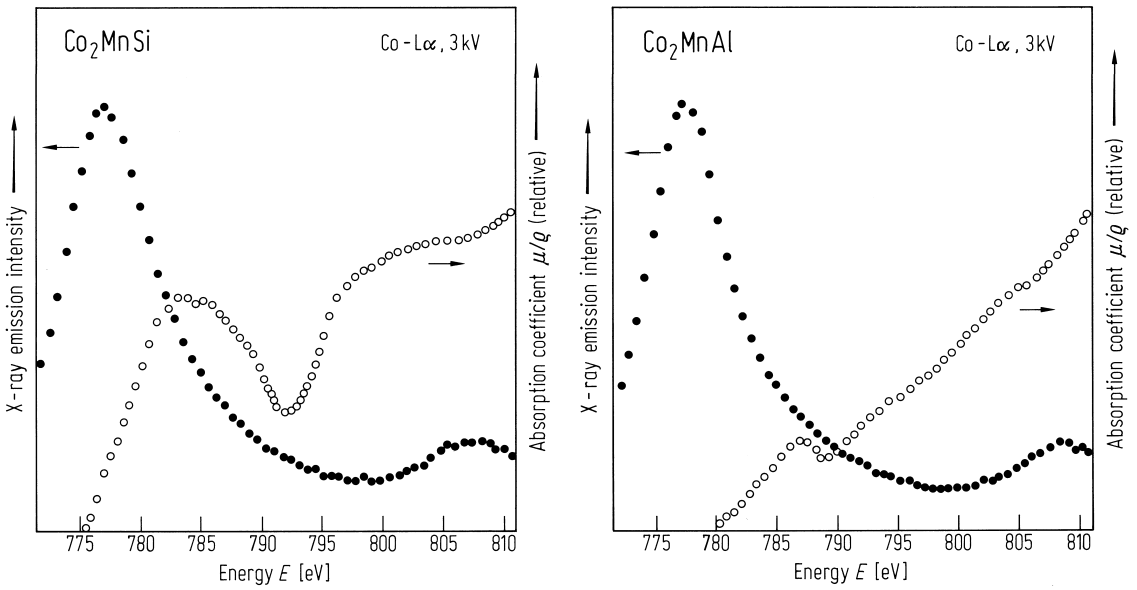

Fig. 573. Observed L_{111} X-ray emission bands and L_{111} self-absorption spectra from Co in Co_2MnSi and Co_2MnAl [83B1].

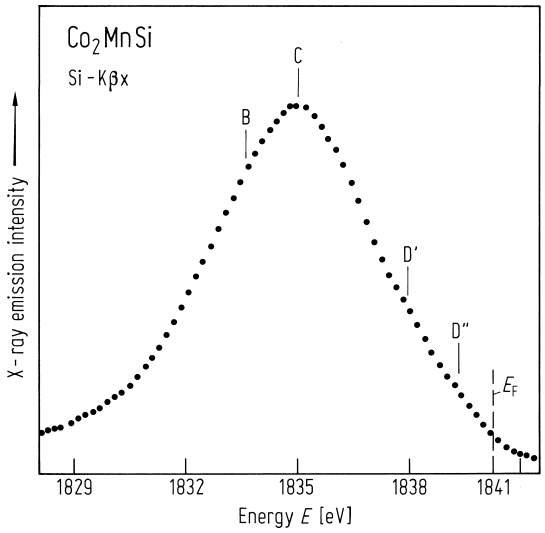

Fig. 572. Observed X-ray emission bands from Si in Co_2MnSi. The bottom of the band is denoted by Γ and the Fermi energy by E_F. The labels B, C and D indicate possible resonant scattering of the nearly free Si electrons by the 3d transition states [83B1].

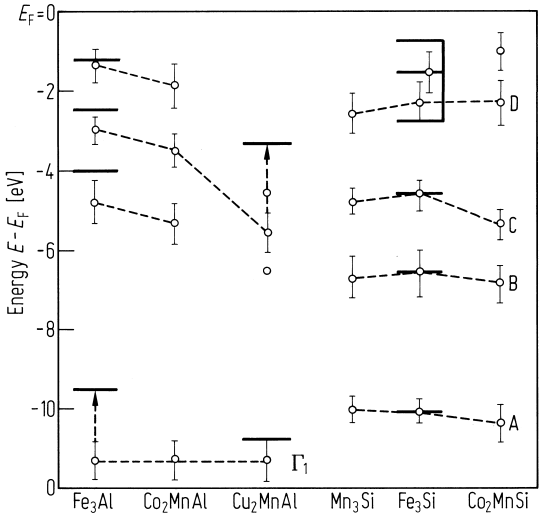

Fig. 575. Schematic energy level scheme for bands DO_3 and $L2_1$ alloys [76S1]. Horizontal bands represent theory [83B1].

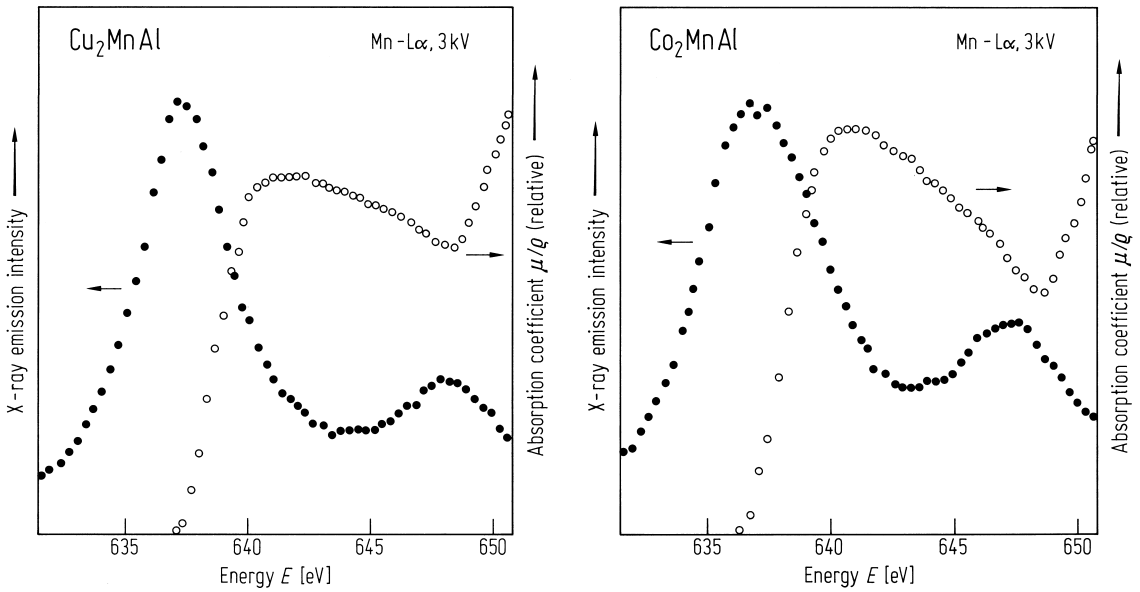

Fig. 574. Observed L_{111} X-ray emission bands and L_{111} self-absorption spectra from Mn in Cu_2MnAl and Co_2MnAl [83B1].

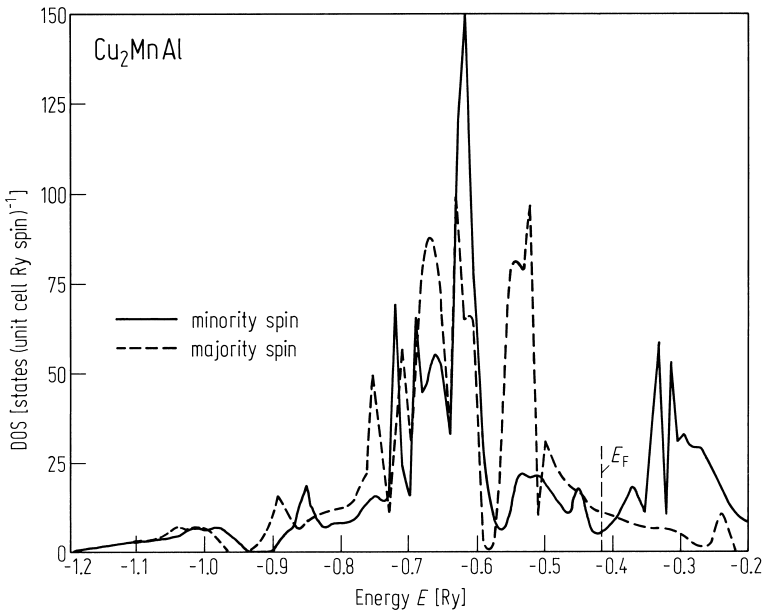

Fig. 576. Spin dependent local and partial density of states for Cu_2MnAl [83B1].

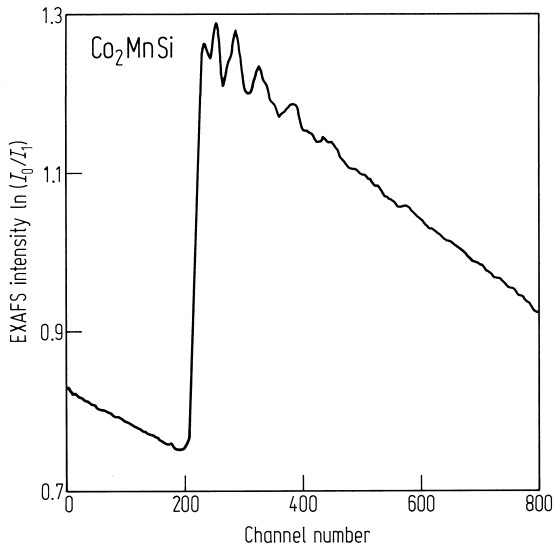

Fig. 577. EXAFS spectrum from Co_2MnSi [84Z1].

X_2YZ X = 4d; Y = 3d

X = 8A: Pd
Y = 4A: Ti
Z = 3B: Al

Photoemission measurements have been made of the intermetallic compound Pd_2TiAl. The valence band extends to a binding energy of 7 eV. Measurements made at the Cooper minimum for Pd 4d indicate that the highest density of states for the Ti 3d is at the Fermi edge and that it decreases towards higher energy. The Pd 4d states also contribute to the Fermi level but the 4d band is not completely full.

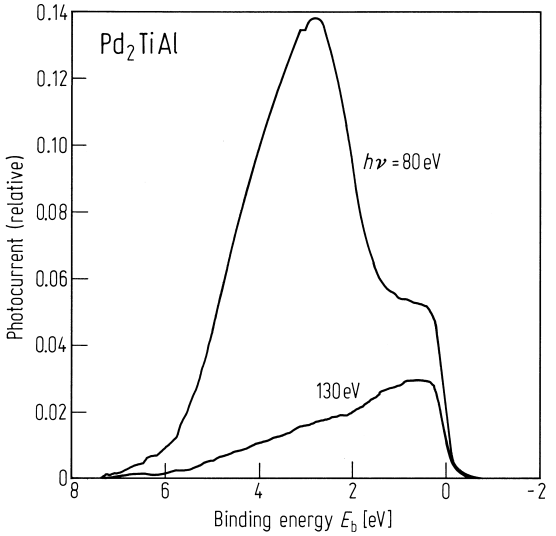

Fig. 579. The background subtracted electron energy distribution curves from Pd_2TiAl for photon energies of 80 eV and 130 eV following correction for the difference in Ti 3d photoemission cross-section between the two photon energies. 130 eV corresponds to the Cooper minimum for Pd 4d photoemission [96L1].

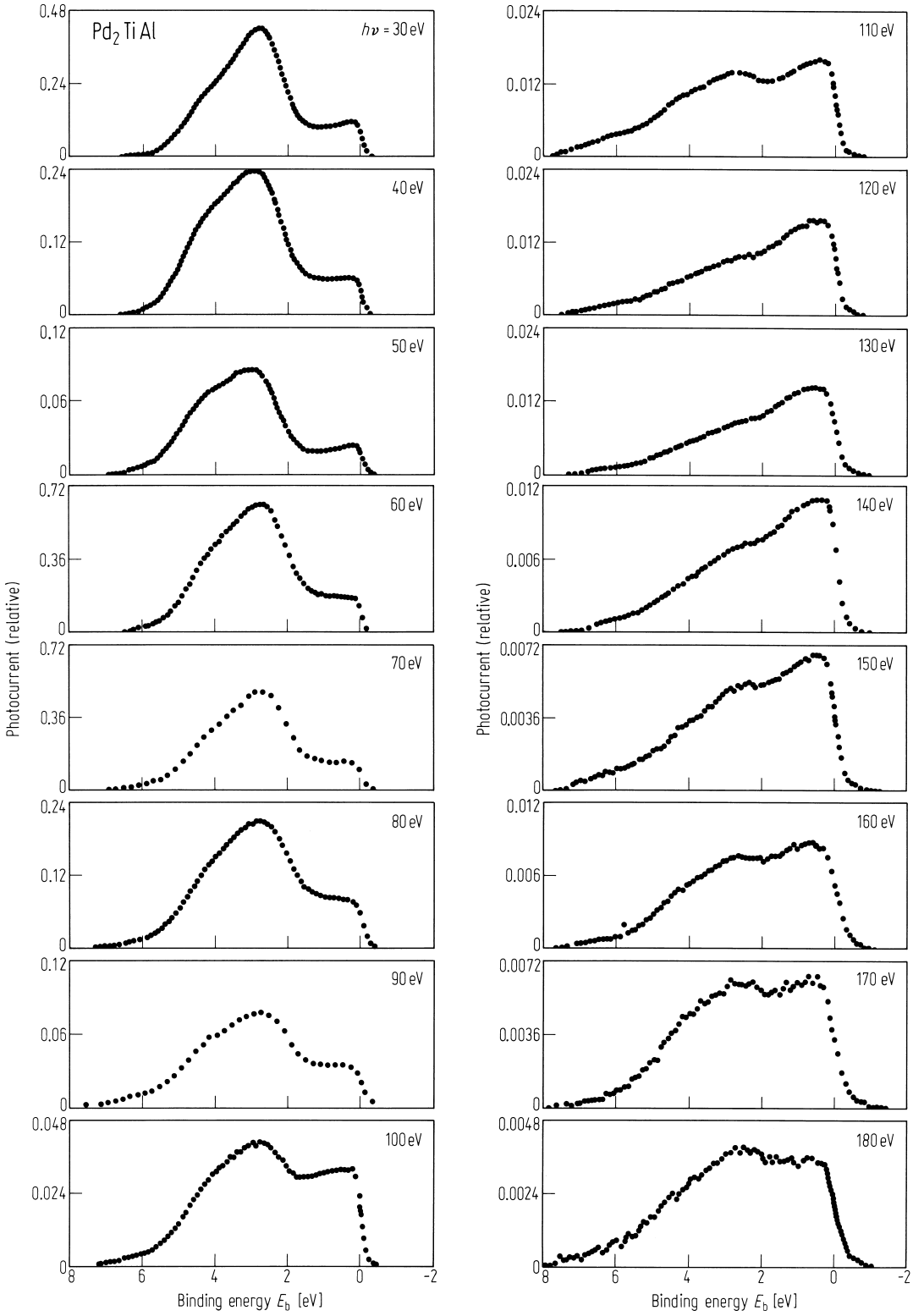

Fig. 578. Electron energy distribution curves collected from Pd_2TiAl for photon energies between 30 and 180 eV. The curves have had the inelastic background subtracted [96L1].

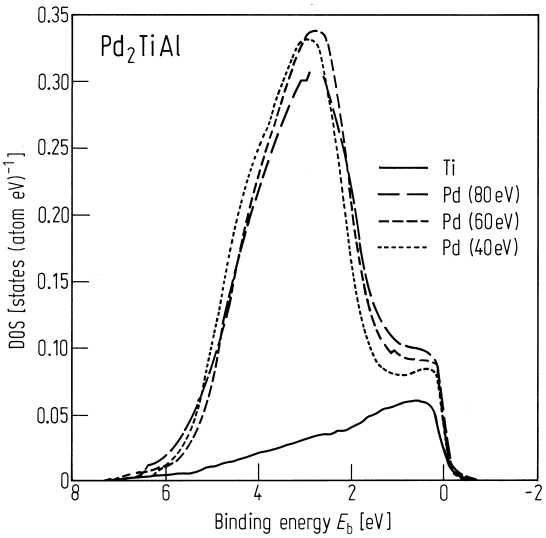

Fig. 580. The experimental density of states Ti 3d and Pd 4d in Pd_2TiAl determined from spectra collected at three different photon energies, assuming Ti $3d^2$, Pd $4d^{10}$ [96L1].

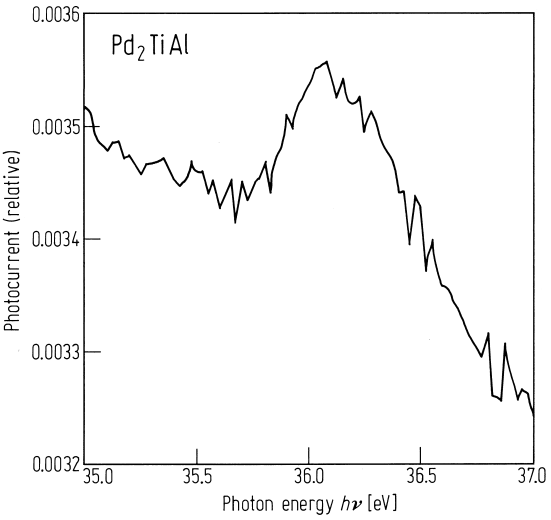

Fig. 582. Constant initial state measurement of the photocurrent obtained from a binding energy of 0.6 eV from Pd_2TiAl, in the photon energy region of the Ti 3p to 3d resonance [96L1].

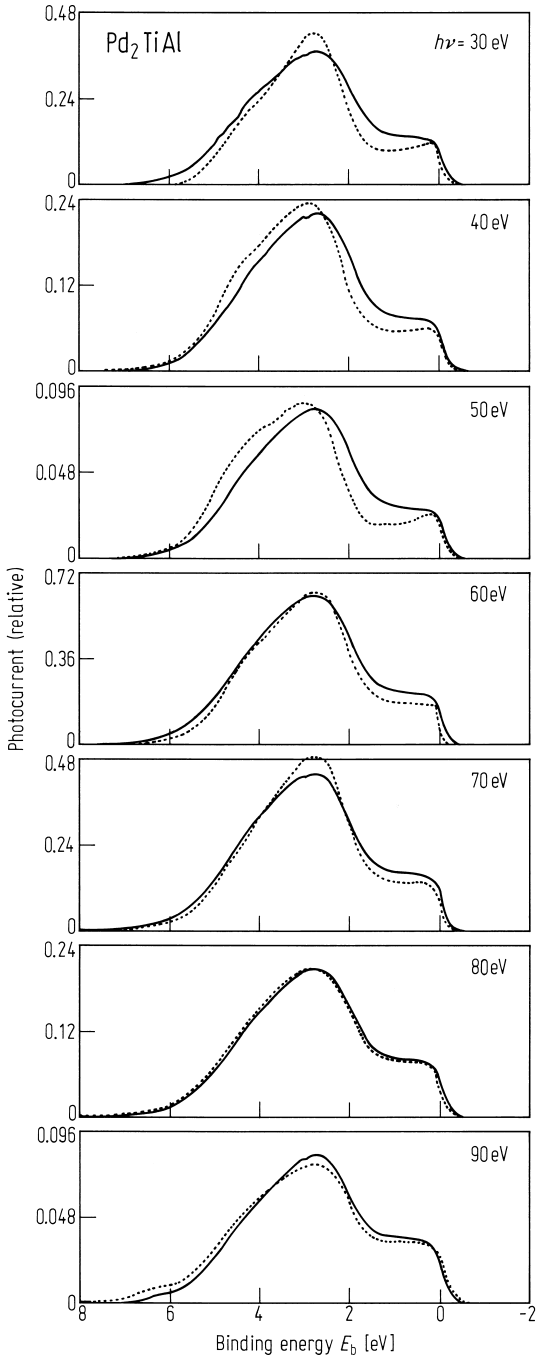

Fig. 581. Comparison of the experimental electron energy distribution curves (dotted) obtained from Pd_2TiAl with those calculated (solid curves) from the DOS determined using Ti $3d^2$, Pd $4d^{10}$ [96L1].

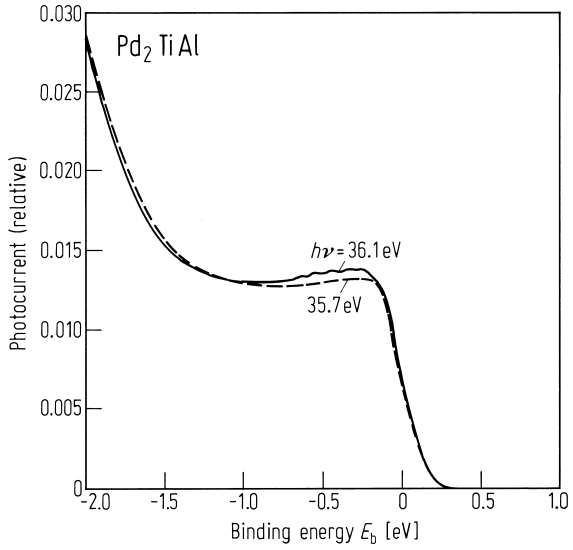

Fig. 583. Background subtracted electron energy distribution curves from Pd_2TiAl collected at photon energies just below the Ti 3p to 4d resonance (35.7 eV) and at the resonance maximum (36.1 eV) [96L1].

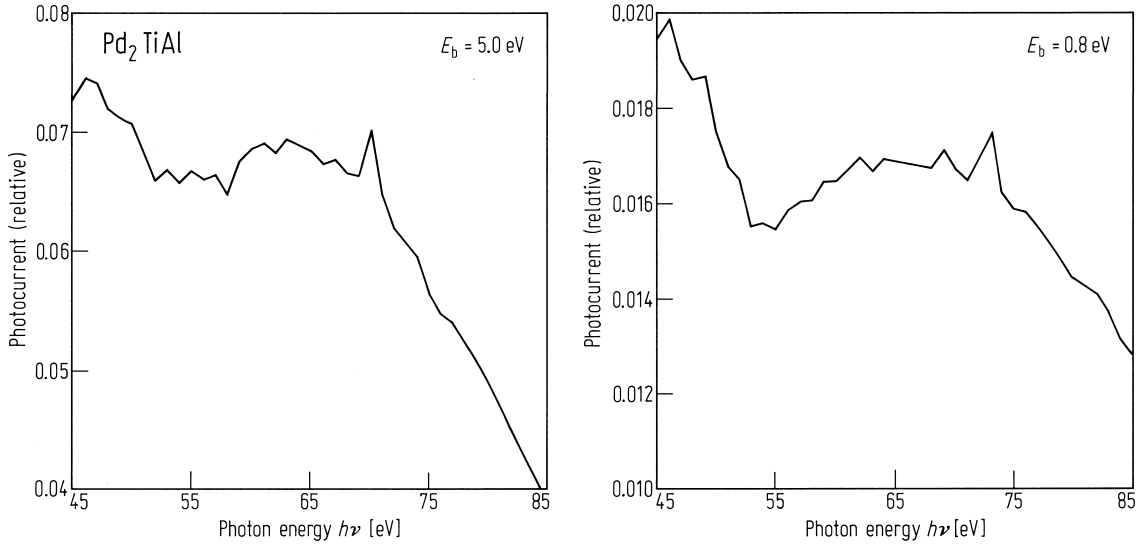

Fig. 584. Constant initial state measurements of Pd_2TiAl made at binding energies of 0.8 and 5 eV for the energy range 45-85eV [96L1].

$C1_bXYZ$ X = 3d Y = 3d

X = 8A: Ni
Y = 7A: Mn
Z = 5B: Sb

Interest in NiMnSb is primarily focused on the prediction that it is a half metallic ferromagnet. [88D1]. The band structure consists of a metallic majority-spin and a semiconducting minority-spin band. The majority-spin Fermi surface consists of three Γ centred hole sheets, two of which have necks at L. The different nature of the bands is clearly reflected in the spin-dependent momentum densities. From these densities a magnetic difference effect in the angular correlation should be clearly visible with polarised positrons. As yet only preliminary results have been reported.

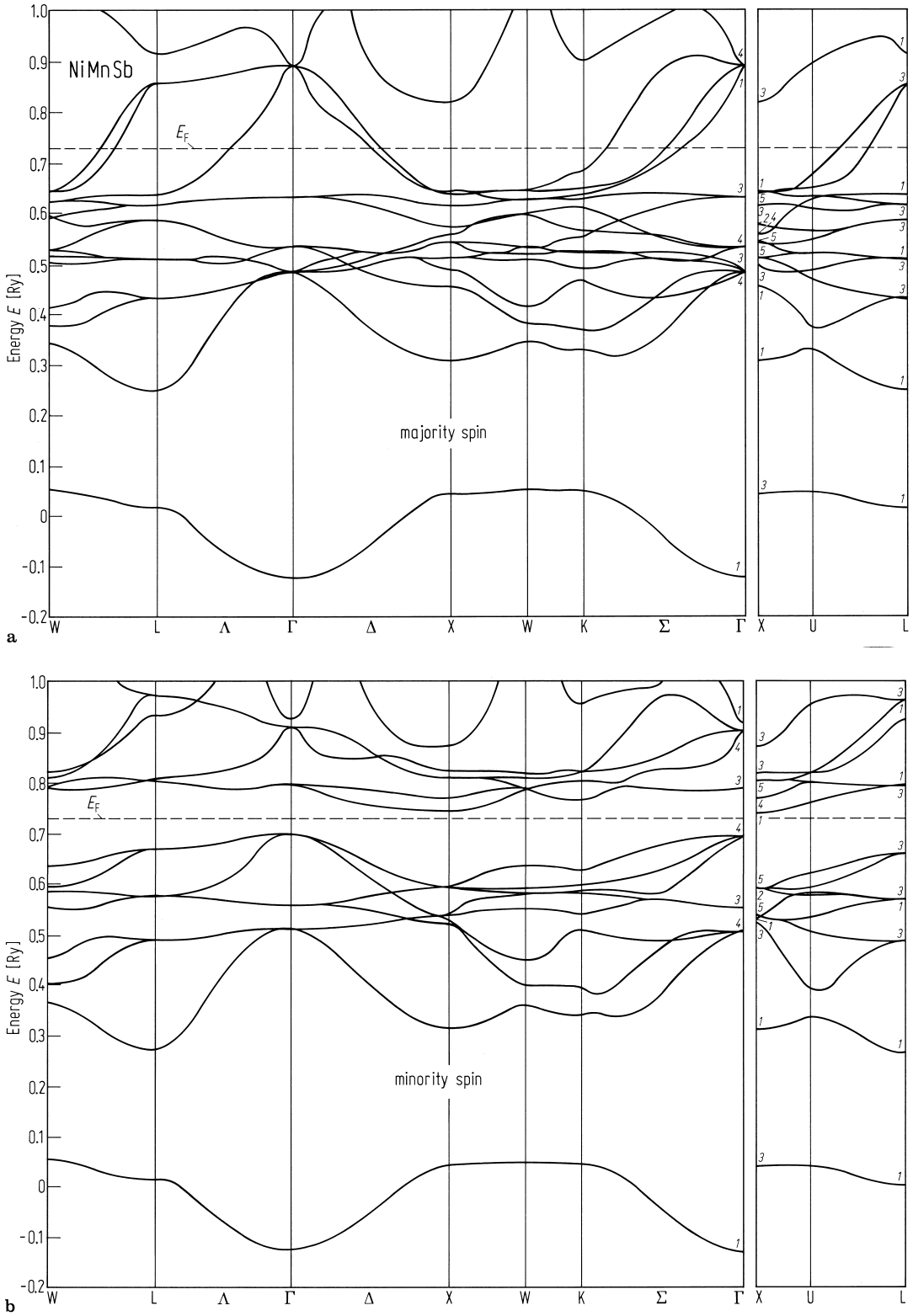

Fig. 585. Band structure for (**a**) the majority-spin and (**b**) the minority-spin electron population in NiMnSb [86H1]. Dashed line indicates E_F.

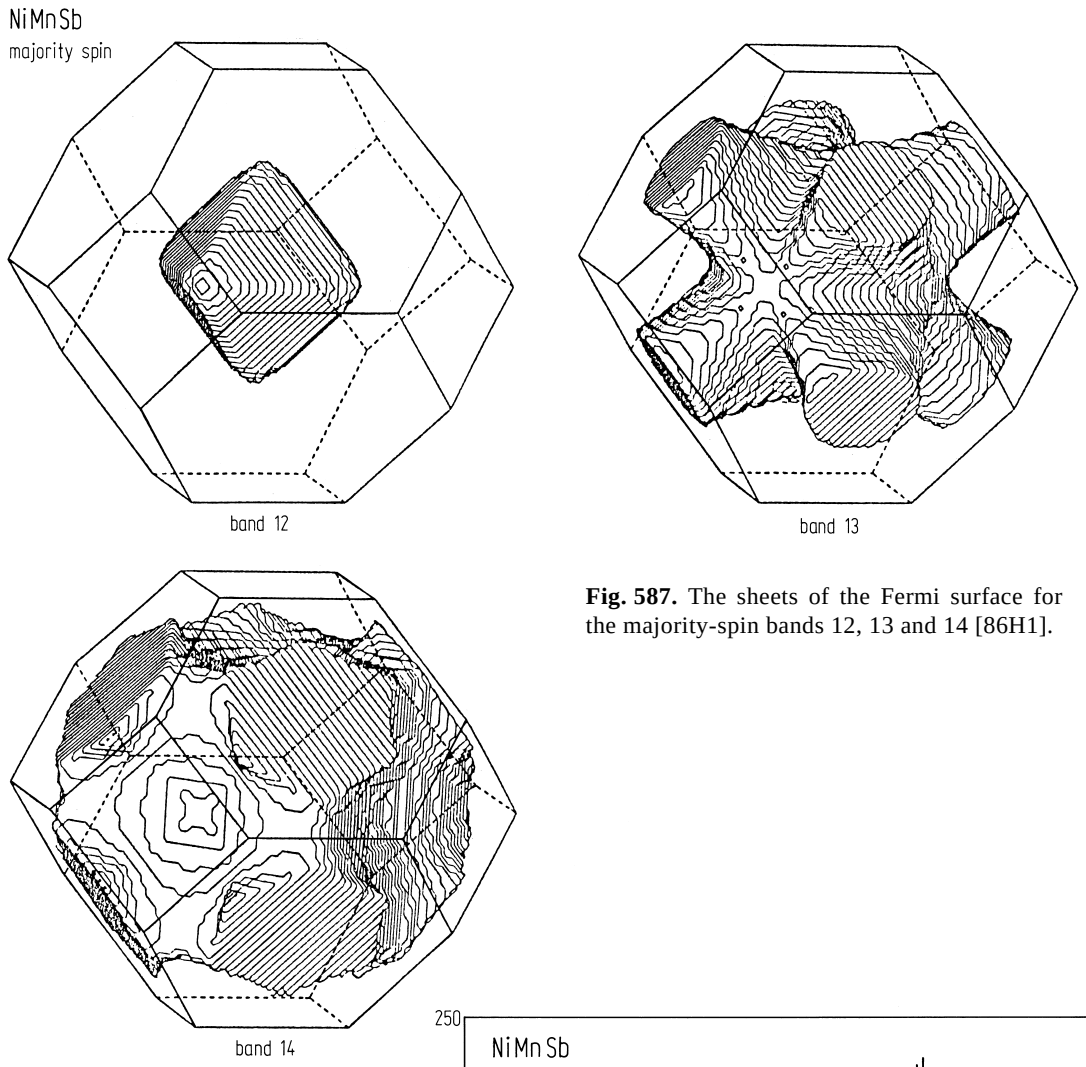

Fig. 587. The sheets of the Fermi surface for the majority-spin bands 12, 13 and 14 [86H1].

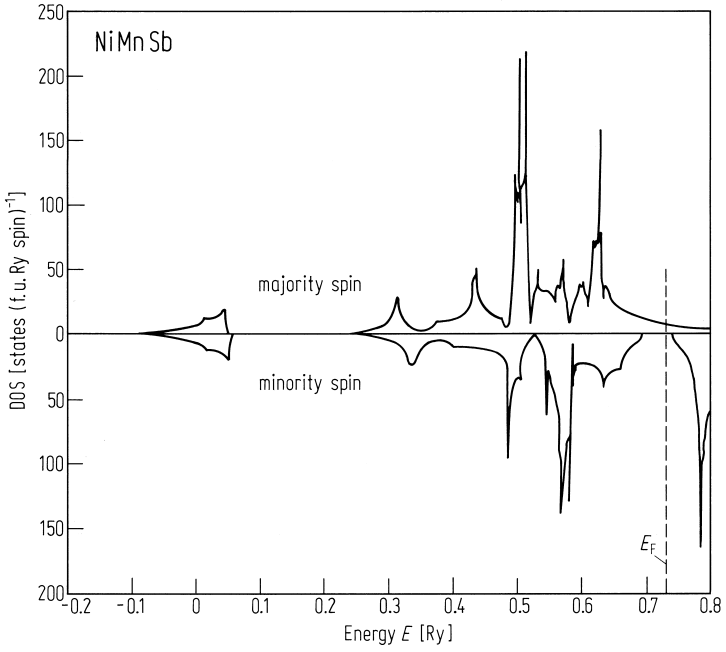

Fig. 586. Total density of states of NiMnSb for the majority-spin and minority-spin direction [86H1].

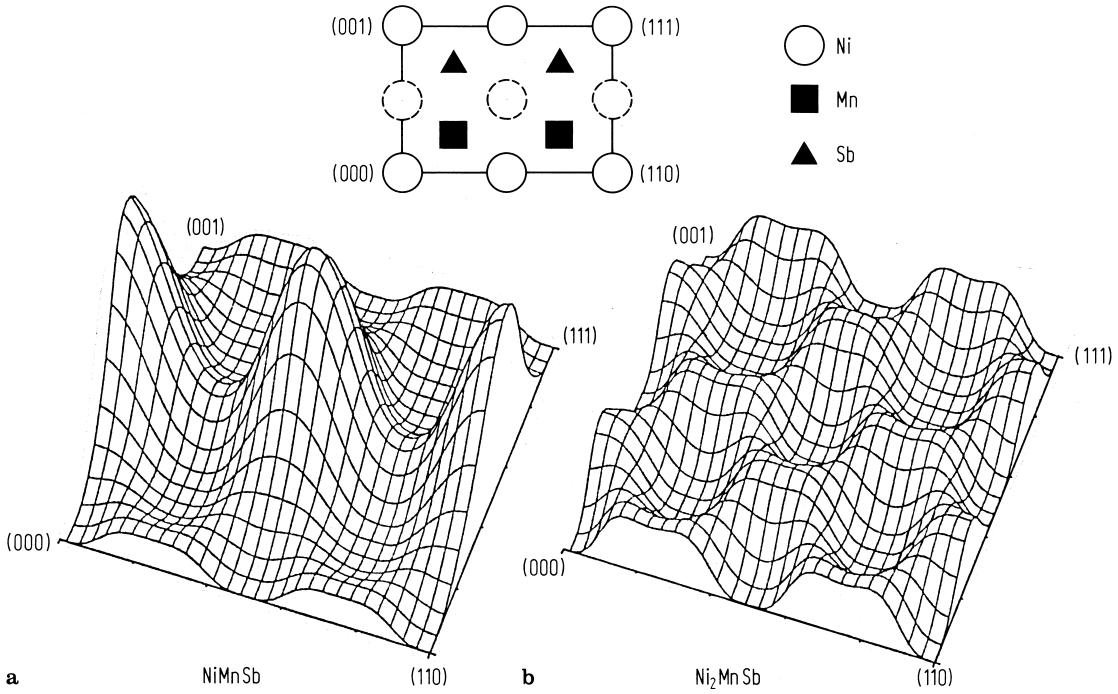

Fig. 588. (**a**) Positron probability density $|\varphi_x r^2|$ in the (110) planes of NiMnSb. The high peaks correspond to the empty lattice positions of the atoms (see inset). (**b**) Same for Ni_2MnSb obtained by placing additional Ni atoms at the empty lattice positions (dashed in the inset) of NiMnSb [86H1].

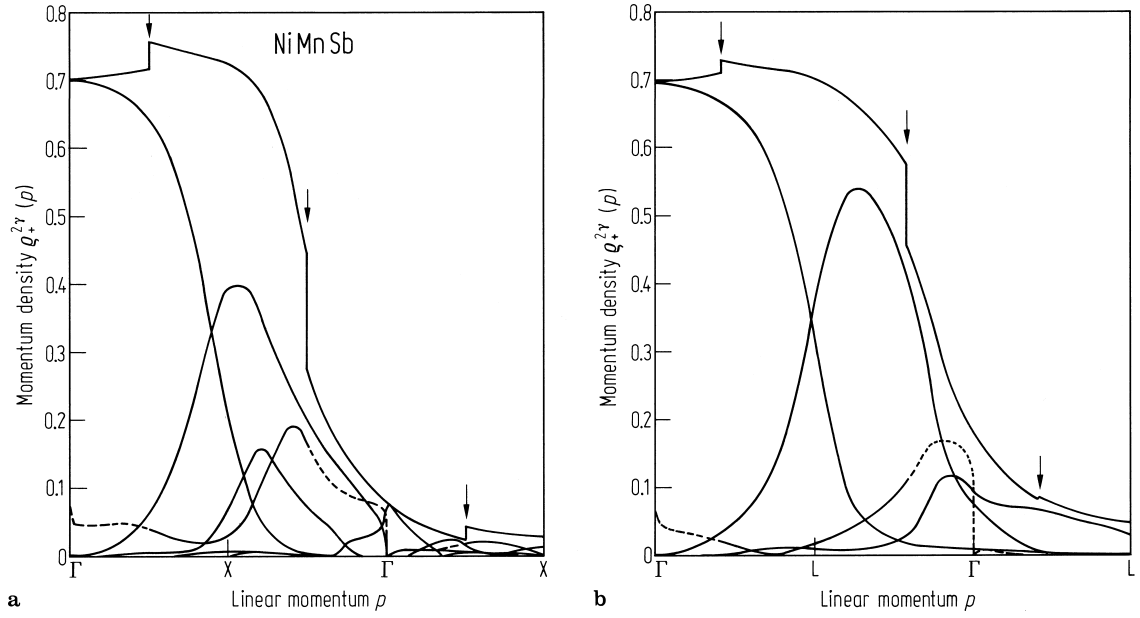

Fig. 589. (**a**) Momentum density of annihilation photon pairs along the direction ΓX for positrons annihilating with the majority-spin electrons in NiMnSb. The dashed curves correspond to un-occupied states and the thick curves give the total of all bands. The arrows indicate the Fermi breaks. (**b**) Same for ΓL [86H1].

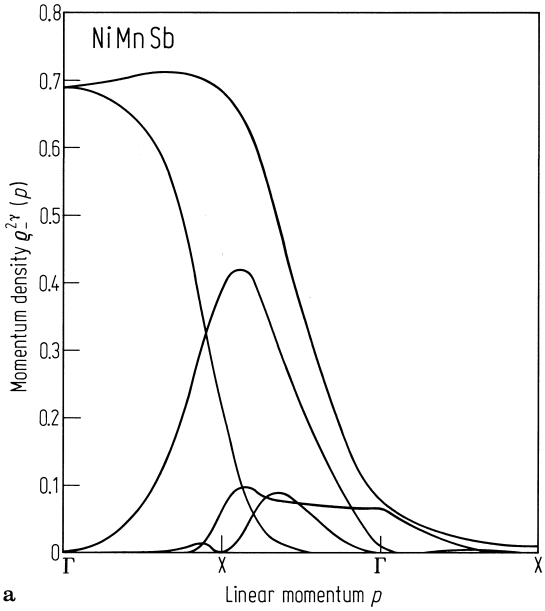

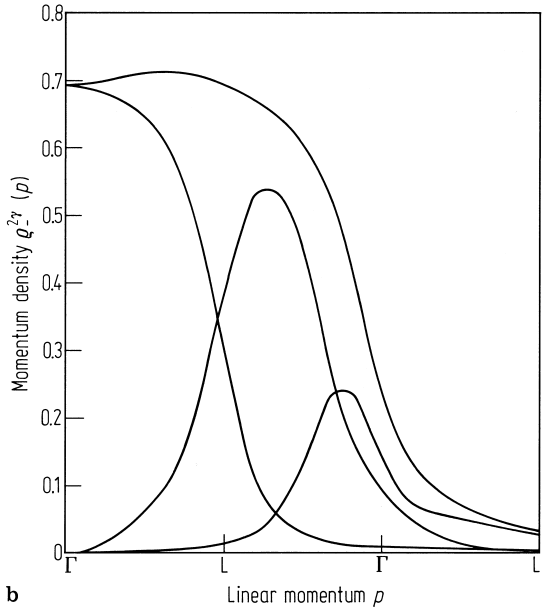

Fig. 590. (**a**) Momentum density of annihilation photon pairs along the direction ΓX for positrons annihilating with the minority-spin electrons in NiMnSb. (**b**) Same for ΓL [86H1].

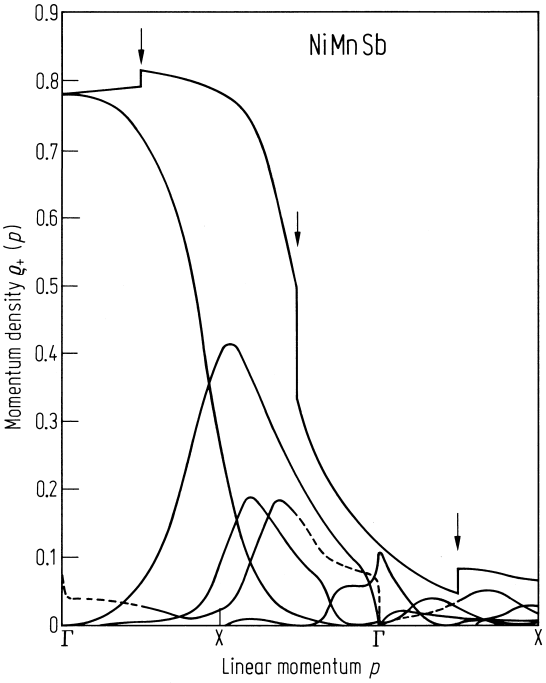

Fig. 591. Momentum density for Compton scattering of the majority-spin electrons along ΓX in NiMnSb [86H1].

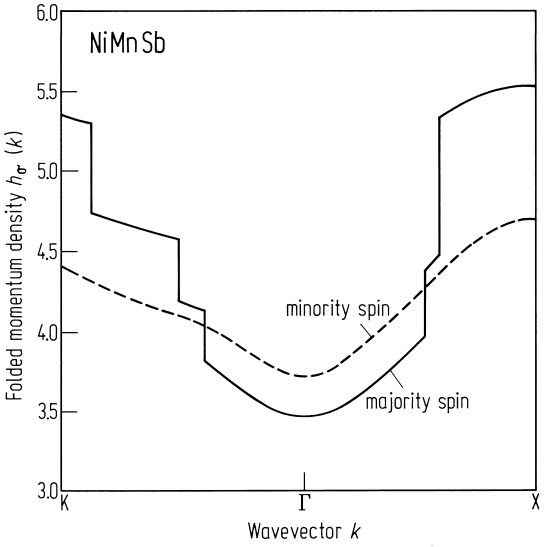

Fig. 592. Folded momentum density of annihilation photon pairs along ΓX and ΓK for annihilation with the majority-spin and minority-spin electrons in NiMnSb [86H1].

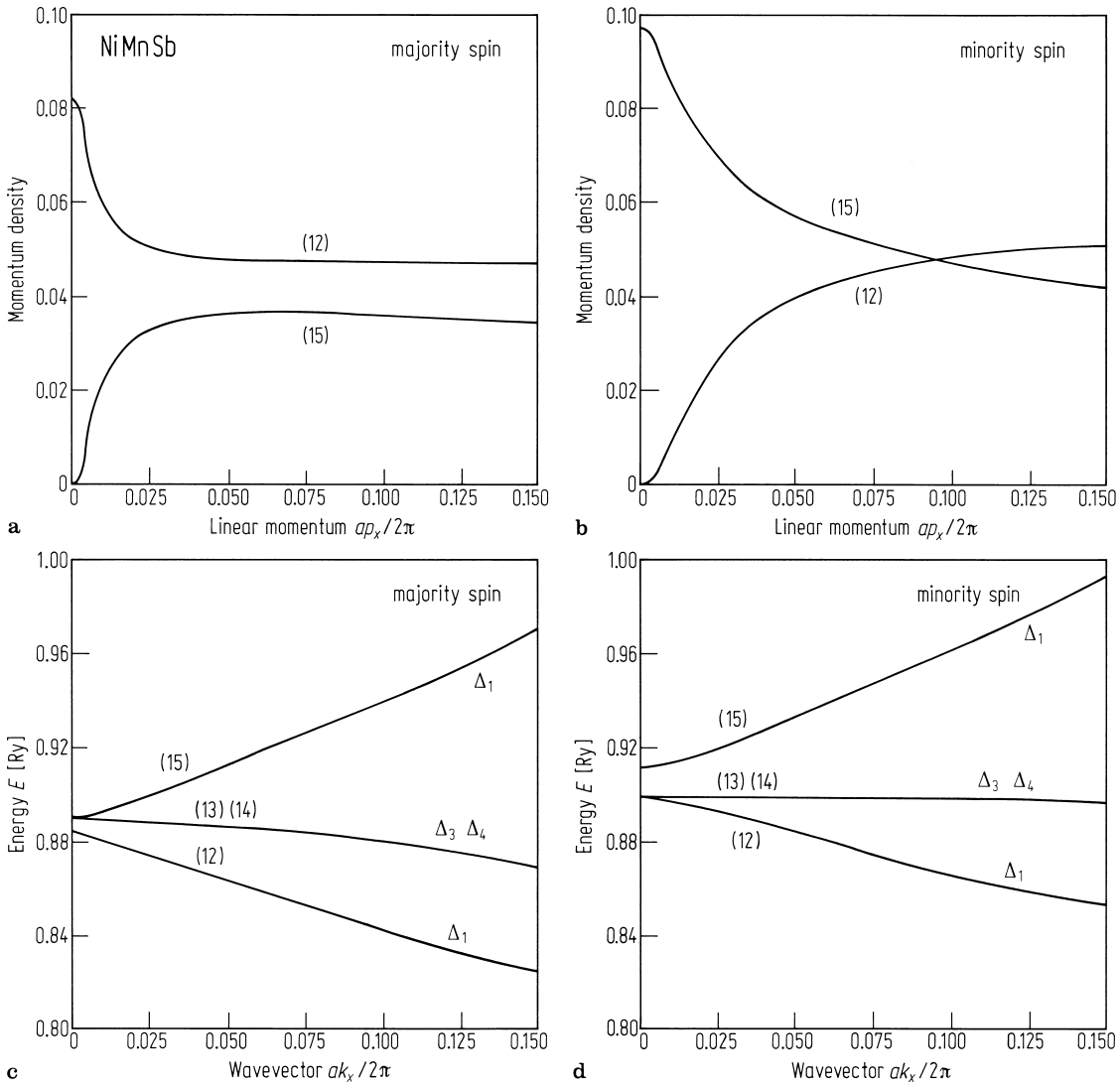

Fig. 593. Momentum density of annihilation photon pairs and band structure in NiMnSb for bands 12 to 15 along ΓX in the neighbourhood of $p = 0$ for (**a**), (**c**) and the majority-spin electrons and (**b**), (**d**) and minority-spin electrons. Band indices are given within parentheses [86H1].

Table 122. Observability of energy bands for momenta $\boldsymbol{p}$ in the T_d^2 lattice. $\boldsymbol{p}$ stands for all vectors related by cubic symmetry, a minus sign indicates a zero contribution to $\rho(\boldsymbol{p})$, a plus sign a non-vanishing contribution to $\rho(\boldsymbol{p})$, • means there is no reciprocal-lattice vector connecting the wavevector $\boldsymbol{k}$ of the symmetry type in the first column to this type of $\boldsymbol{p}$ vector, and ξ, η and ξ are all different and nonzero [86H1].

Energy band	p_x	0	0	0	ξ	0	ξ	ξ
	p_y	0	0	ξ	ξ	ξ	η	η
	p_z	0	ξ	ξ	ξ	η	η	ξ
Γ_1		+	+	+	+	+	+	+
Γ_2		–	–	–	–	+	–	+
Γ_3		–	+	+	–	+	+	+
Γ_4		–	+	+	+	+	+	+
Γ_5		–	–	+	–	+	+	+
X_1, X_3		•	+	+	•	+	+	+
X_2, X_4		•	–	–	•	+	–	+
X_5		•	–	+	•	+	+	+
W_1, W_2, W_3, W_4		•	•	•	•	+	+	+
Σ_1, S_1		•	•	+	•	+	+	+
Σ_2, S_2		•	•	–	•	+	–	+
L_1, Λ_1		•	•	•	+	•	+	+
L_2, Λ_2		•	•	•	–	•	–	+
L_3, Λ_3		•	•	•	–	•	+	+
Δ_1		•	+	•	•	+	+	+
Δ_2, Δ_4		•	–	•	•	+	–	+
Δ_3		•	–	•	•	+	+	+
V_1, V_2		•	•	•	•	+	•	+

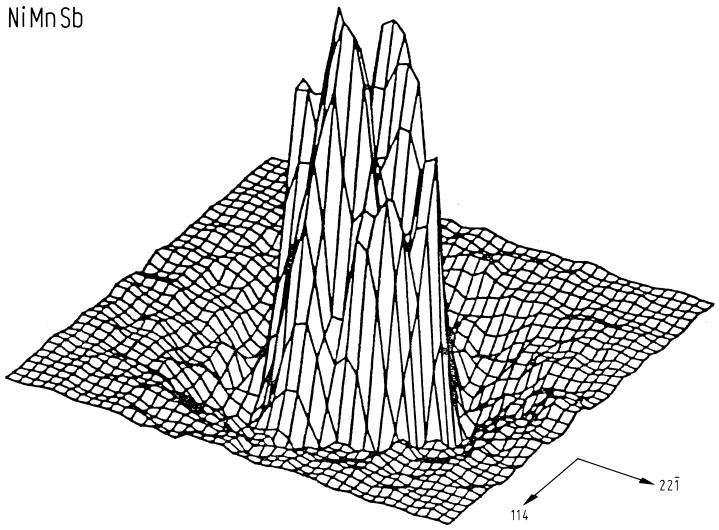

Fig. 594. Measured two-dimensional spin density $\Delta N(p_y, p_z) = \int\left[\rho_-^{2\gamma}(\boldsymbol{p}) - \rho_+^{2\gamma}(\boldsymbol{p})\right] \mathrm{d}p_x$ in the (ITO) plane in NiMnSb not corrected for the momentum sampling function. Each division is 10^{-3} mc [84M1].

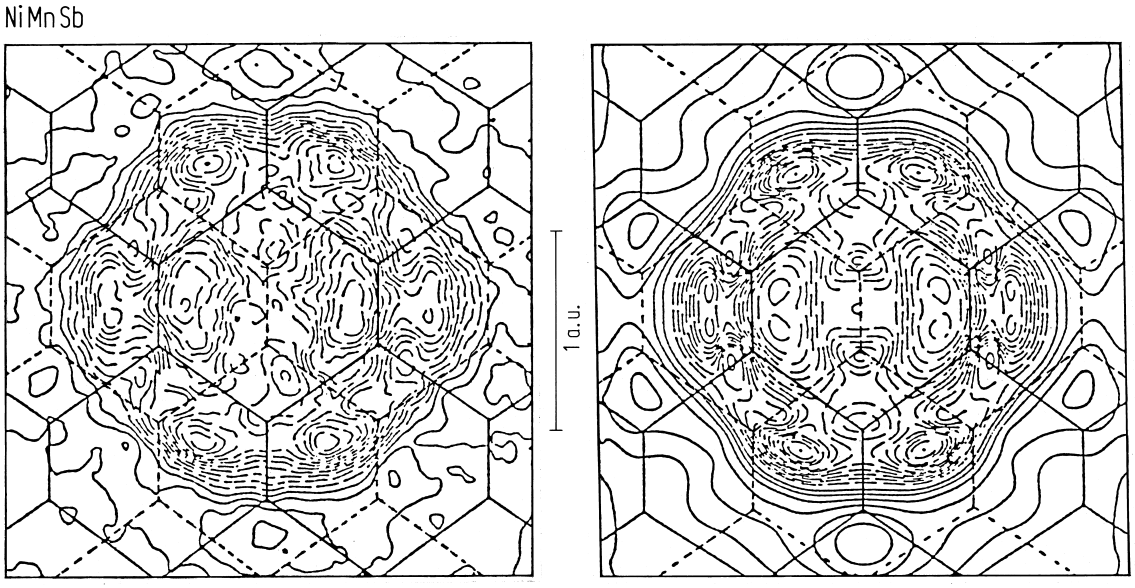

Fig. 595. Difference between the ([110]-integrated) momentum densities of minority and majority spin electrons in NiMnSb, measured with polarised positrons. Left: experiment, right: theory [88M1].

1.5.5.11 Magneto-optics

The response of a medium to electric and magnetic fields is determined by the permittivity and permeability tensors $\boldsymbol{\varepsilon}$ and $\boldsymbol{\mu}$, respectively. For time dependent fields (and in particular for electromagnetic radiation) and for dielectric materials, it is the refractive index n which fully characterises the optical properties. The elements of $\boldsymbol{\varepsilon}$ may be complex and are related to the refractive index by an equation of the form $\boldsymbol{\varepsilon}_{xx} = \left(n_{xx} + \mathrm{i}n'_{xx}\right)^2$. Here $n_{xx}(n'_{xx})$ is the real (imaginary) part of the refractive index n.

For an isotropic material the permittivity is a diagonal tensor. However, if the material is magnetised the macroscopic orientation of the magnetisation singles out a unique direction. As a consequence the permittivity tensor acquires off-diagonal elements which are, to first order, linear in the magnetisation $\boldsymbol{M}$. Thus the permittivity tensor has the form:

$$\boldsymbol{\varepsilon} = \begin{pmatrix} \varepsilon_{xx} & \pm i\varepsilon_{xy} & 0 \\ \mp i\varepsilon_{xy} & \varepsilon_{xx} & 0 \\ 0 & 0 & \varepsilon_{zz} \end{pmatrix}$$

for a magnetisation M which is directed along the z axis ($\boldsymbol{M}||\boldsymbol{z}$). The off-diagonal matrix element is often parameterized in the form

$$Q = \frac{\varepsilon_{xy}}{\varepsilon_{xx}}$$

with Q being the magneto-optic parameter. Q or ε_{xy} change sign if the direction of the magnetisation is reversed. In the literature different sign conventions are in use. For a discussion of the question of the sign convention in magneto-optical calculations and measurements the interested reader is referred to [93A1].